

**REPUBLIC OF TURKEY  
YILDIZ TECHNICAL UNIVERSITY  
GRADUATE SCHOOL OF NATURAL AND APPLIED SCIENCES**

**THE EFFECT OF GRAVITATIONAL CLUSTERING ON THE  
GALAXY EVOLUTION**

**TURGAY AĐLAR**

**MSc. THESIS  
DEPARTMENT OF PHYSICS  
PROGRAM OF PHYSICS**

**ADVISER  
ASSIST. PROF. DR. MURAT HÜDAVERDİ**

**İSTANBUL, 2016**

**REPUBLIC OF TURKEY**  
**YILDIZ TECHNICAL UNIVERSITY**  
**GRADUATE SCHOOL OF NATURAL AND APPLIED SCIENCES**

**LOCATION ANALYSIS OF THE EMERGENCY SERVICE  
CENTERS OF A CASE COMPANY**

A thesis submitted by Turgay CAGLAR in partial fulfillment of the requirements for the degree of **MASTER OF SCIENCE** is approved by the committee on 01.03.2013 in Department of Physics.

**Thesis Adviser**

Assist. Prof. Dr. Murat HÜDAVERDİ  
Yıldız Technical University

**Approved By the Examining Committee**

Assist. Prof. Dr. Murat HÜDAVERDİ  
Yıldız Technical University

\_\_\_\_\_

Assoc. Prof. Dr. Taylan YETKİN  
Yıldız Technical University

\_\_\_\_\_

Prof. Dr. E. Nihal ERCAN  
Bogazici University

\_\_\_\_\_

This study was supported by the BAPK Grant No: 2013-01-01-YL01

This study was supported by the Scientific and Technological Research Council of Turkey (TUBITAK) Grant No: 113F117

## ACKNOWLEDGEMENTS

---

First and foremost, I have to thank my research supervisor, Assistant Prof. **Murat HÜDAVERDİ**. Without his assistance and dedicated involvement in every step throughout the process, this paper would have never been accomplished. I would like to thank you very much for your support and understanding over these past four years.

I would also like to show gratitude our laboratory partners, including **Cemile EZER**, **Ebru AKTEKİN**, **Hakan SERT** and **Muhammed Kıyami ERDİM**.

In June 2014, I went to European Space agency for several days to participate Xmm Sas Workshop. My time at ESA has been highly productive and working with Mr. **Ignacio de la CALLE** was an extraordinary experience. Prof. Dr. **Kubilay KUTLU** was my first-year Quantum Mechanics lecturer at Yildiz Technical University. His teaching style and enthusiasm for the topic made a strong impression on me and I have always carried positive memories of his classes with me.

Getting through my dissertation required more than academic support, and I have many, many people to thank for listening to and, at times, having to tolerate me over the past three years. I'd like to thank my friends **Cihan AYTULUN**, **Metin UZUNOĞLU** for their helps and supports whenever I require. For many memorable evenings out and in, I must thank **Serdar ÖZCAN** for frequent chats at unreasonable hours. I must also thank **Hasan Lütfü ÖRSDEMİR** and **Eymen KULLUKÇU** for supplying a great ambient to hang out.

Most importantly, none of this could have happened without my family. Many thanks with huge hugs go to my dear mother. She has always been there for me whenever I needed. I'd like to thank my sister and my father for their unlimited support during my thesis period.

January, 2016

Turgay ÇAĞLAR

## TABLE OF CONTENTS

---

	Page
LIST OF SYMBOLS .....	vii
LIST OF ABBREVIATIONS.....	viii
LIST OF FIGURES .....	ix
LIST OF TABLES.....	x
ABSTRACT.....	xi
ÖZET .....	xii
CHAPTER 1	
INTRODUCTION .....	1
1.1 Literature Review .....	1
1.1.1 Formation of the Universe .....	1
1.1.2 Clusters of Galaxies .....	1
1.1.3 Galaxies .....	2
1.1.4 Intra Cluster Medium.....	3
1.2 Objective of Thesis .....	4
1.3 Hypothesis .....	5
CHAPTER 2	
XMM NEWTON .....	6
2.1 Spacecraft.....	6
2.1.1 Components .....	6
2.1.2 Structural Design .....	8
2.1.3 Thermal Constant.....	8
2.2 Mirrors .....	9
2.2.1 Introduction.....	9
2.2.2 Telescope Configuration.....	9
2.2.3 Optical Design .....	10
2.2.4 Image Quality .....	11

2.2.5	Effective Area .....	11
2.2.6	X-Ray Straylight Rejection.....	12
2.3	EPIC.....	12
2.3.1	Introduction.....	12
2.3.2	Chip Geometry.....	13
2.3.3	Operating Modes.....	14
2.3.4	Instrumental Characteristic .....	15
 CHAPTER 3		
OBSERVATION AND DATA REDUCTION.....		16
3.1	Motivation and Source Selection .....	16
3.2	Observation.....	17
3.3	Data Reduction .....	17
3.4	Background Selection .....	17
 CHAPTER 4		
ANALYSIS.....		18
4.1	Overview.....	18
4.1.1	Abell 3581.....	18
4.1.2	Abell 400.....	18
4.2	X-Ray Images .....	19
4.2.1	Abell 3581 ICM Shape .....	20
4.2.2	Abell 400 ICM Shape .....	21
4.3	Source Detection.....	22
4.4	Log N - Log S .....	23
4.4.1	Solid Angle of the Survey.....	23
4.4.2	Cumulative Source Counts Per Degree Square .....	24
 CHAPTER 5		
RESULTS AND DISCUSSION.....		25
REFERENCES .....		28
 APPENDIX-A		
ABELL 3581.....		30
 APPENDIX-B		
ABELL 400.....		32
CURRICULUM VITAE.....		33

## LIST OF SYMBOLS

---

$\rho_g$	Density
$L_\odot$	Solar Luminosity
$\Omega_i$	Sky Coverage
$H_0$	Hubble Constant
$q_0$	Deceleration Parameter
$z$	Redshift
$n_H$	Hydrogen Column Density

## LIST OF ABBREVIATIONS

---

AGN	Active Galactic Nuclei
CCD	Charged Coupled Device
CD	Central Dominant
ECF	Energy Conversion Factor
ICM	Intra Cluster Medium

## LIST OF FIGURES

---

	Page
Figure 1.1 Coma Cluster, X-ray (Red) Optic (White).....	4
Figure 1.2 Hydrostatic Equilibrium of a Spherical Object.....	4
Figure 2.1 X-ray Telescope of XMM Newton.....	7
Figure 2.2 XMM Newton Spacecraft.....	7
Figure 2.3 Mirror Interface of Structure.....	10
Figure 2.4 Chip Geometries of Cameras.....	14
Figure 4.1 True Color Image of Abell 3581.....	19
Figure 4.2 True Color Image of Abell 400.....	19
Figure 4.3 MOS1 ICM Image of Abell 3581.....	20
Figure 4.4 MOS2 ICM Image of Abell 3581.....	20
Figure 4.5 PN ICM Image of Abell 3581.....	20
Figure 4.6 Mosaic Image of Abell 3581.....	21
Figure 4.7 MOS1 ICM Image of Abell 400.....	21
Figure 4.8 MOS2 ICM Image of Abell 400.....	21
Figure 4.9 PN ICM Image of Abell 400.....	22
Figure 4.10 Mosaic Image of Abell 400.....	22
Figure 4.11 Detected Sources of Abell 3581 and Abell 400 Respectively.....	23
Figure 5.1 Log N – Log S distributions of Abell 3581 and Abell 400.....	36
Figure 5.2 X-ray to Optical Luminosity Distributions of Abell 3581 and Abell 400.....	27

## LIST OF TABLES

---

	Page
Table 5.1 X-ray and Optical Values.....	27
Table A.1 Abell 3581 Results.....	30
Table B.1 Abell 400 Results.....	32

## ABSTRACT

---

# THE EFFECT OF GRAVITATIONAL CLUSTERING ON THE GALAXY EVOLUTION

Turgay AĐLAR

Department of Physics

MSc. Thesis

Adviser: Asist. Prof. Dr. Murat HÜDAVERDİ

With the advent of the technology in space science we are now spatially and spectrally able to resolve hot dense plasma emissions from far edges of the universe. Thanks to XMM-Newton (ESA) and Chandra (NASA) satellites, now we can study the mysteries of the cosmos with up to 5 arcsec spatial and several eV spectral energy resolutions. In this work we have selected two clusters of galaxies Abell 400 and Abell 3581 clusters of galaxies with moderate distant ( $z < 0.025 \sim 105 \text{Mpc}$ ) in order to understand possible mutual interactions of extend intra cluster medium and galaxies within the clusters itself. Since each galaxy has different physical properties, we have applied a multi-band source detection technique to identify all types of point like sources within the field of view. We detect 64 X-ray point sources by EPIC-PN camera of XMM-Newton satellite of ESA. The detected sources are compared with Lockman-Hole field galaxies. The integrated number of sources as a function of flux,  $\text{Log}(N)$ -  $\text{Log}(S)$  measured between 2-10 keV. We classified statistically insufficient sources according to X-ray color diagram. The luminosity range is faint ( $39.7 < \log(L_x) < 41.75$  ergs/s), which is probably polluted by low-mass X-ray binaries (LMXBs), hot halo, and low luminous active nuclei. Based on our preliminary results, we observe an enhanced X-ray emission from galaxies from the cluster fields; in other words they are significantly brighter in X-rays. Possible physical mechanisms are discussed to explain to current situation.

**Key words:** Galaxy, Hot Plasma, Clusters of Galaxies, X-rays, satellite

---

YILDIZ TECHNICAL UNIVERSITY  
GRADUATE SCHOOL OF NATURAL AND APPLIED SCIENCES

## ÖZET

---

# ÇEKİMSEL KÜRESELLEŞMENİN GALAKSİ EVRİMİNE ETKİSİ

Turgay ÇAĞLAR

Fizik Bölümü

Yüksek Lisans Tezi

Tez Danışmanı: Asist. Prof. DR. Murat HÜDAVERDİ

Uzay bilimlerinde ki teknolojik gelişmelerle birlikte artık uzayın uzak uçlarında ki sıcak plazma yayılımları ile ilgili kesin kararlar verebiliyoruz. Nasa'nın Chandra ve Esa'nın XMM-Newton uydularındaki yüksek çözünürlüklü kameralar sayesinde, artık evrenin sınırlarını 5 arcsecond uzaklığında ve birkaç ev dolaylarında ki enerji çözünürlüğünde inceleyebiliyoruz. Bu çalışmayı, yakın ( $z < 0.025 \sim 105$  Mpc) iki küme olan A400'e ve A3581'i saran sıcak plazma ile bu kümelere ait galaksilerin arasındaki etkileşimleri anlamak için seçtik. Her galaksi ayrı bir fiziksel özelliğe sahip olduğundan, görüş alanımızda ki nokta kaynakların kimliklerini saptamak için çok bantta nokta kaynak tespiti uyguladık. 64 adet X-ray nokta kaynak ESA'nın XMM-Newton uydusunun EPIC-PN kamerası tarafından tespit edildi. Tespit Edilen Kaynaklar Lockman Boşluğunda ki alan galaksileri ile karşılaştırıldı. Birleştirilmiş kaynaklar akının bir fonksiyonu olarak  $\text{Log}(N)\text{-Log}(S)$  yöntemiyle 2-10 keV aralığında ölçüldü. İstatistiksel olarak yetersiz nokta kaynaklar X-ray renk diyagramına göre sınıflandırıldı. Aydınlık menzili ( $38.7 < \log(L_x) < 41.75 \text{ ergs/s}$ ), büyük ihtimalle küçük kütleli X-ray sistemleri, sıcak hale ve düşük aydınlıkta etkin çekirdekli galaksiler olması dolayısı ile zayıflar. Elde ettiğimiz sonuçlara göre , küme alanındaki galaksilerden X-ray ışımaya gözlemlendi, diğer bir deyişle bu galaksiler X-ray de önemli ölçüde parlaklar.

**Anahtar Kelimeler:** Galaksi, Sıcak Plazma, Galaksi Kümeleri, X-ray, Uydu

---

YILDIZ TEKNİK ÜNİVERSİTESİ FEN BİLİMLERİ ENSTİTÜSÜ

### INTRODUCTION

#### 1.1 Literature Review

##### 1.1.1 Formation of the Universe

Universe has been expanding to its current shape from initial singularity. After formation of first particles, a rapidly cooling universe permits particles to form into more complex systems, such as atoms, elements, clouds, first stars and first galaxies etc. Smaller clouds have been formed into first stars and giant ones has been formed into first galaxies. As first galaxies clustered together under gravity, first stars died and spewed heavy elements into space; they eventually formed into new stars and planets. Since galaxies love to cluster together, the largest gravitationally bound objects of the universe has been formed, namely clusters of galaxies.

##### 1.1.2 Clusters of Galaxies

Clusters of galaxies are the largest structures of the universe that we detected so far and they are next to quasars, the most luminous X-ray sources in the Universe with radiation powers of the order of  $10^{43} - 10^{46} \text{erg s}^{-1}$ . As structure grows hierarchically, clusters of galaxies are the most recently formed gravitationally relaxed systems. Among relaxed systems, they are the most massive, with masses ranging from  $10^{13} M_{\odot}$  to over  $10^{15} M_{\odot}$ . The majority of the mass in a galaxy cluster ( $\approx 80\%$ ), is in the form of invisible non-baryonic dark matter [1],[2]. The remaining baryonic component is mostly in the form of a hot and diffuse intra cluster gas, with small contribution from stars, dust and cold gas.

### 1.1.3 Galaxies

Galaxy is massive, gravitationally bound system consisting of stars, stellar remnants, an interstellar medium of gas and dust and dark matter. Clustering with others is the nature of galaxies, that's why we have galaxy groups and clusters in the universe. A galaxy clusters must have a minimum population of 50 members within a magnitude of  $m_3 + m_3 + 2A$  where  $m_3$  is the magnitude of the 3th brightest member of the galaxy clusters. A galaxy cluster may contain a few tens to thousands of galaxies that are bound in the gravitational potential of cluster and move randomly in the clusters. Abell [3] classified galaxy clusters according to their richness class. Richness class of a galaxy cluster can be defined as number of the galaxy cluster members. Abell's classifications are divided clusters into six 'richness class':

Class 0: 30-49 galaxies

Class I: 49-79 galaxies

Class II: 80-129 galaxies

Class III: 130-199 galaxies

Class IV: 200-299 galaxies

Our Milky Way is part of poor cluster called as Local Group. It has two large spirals, one small spiral, two ellipticals, 13 irregulars and 14 dwarf ellipticals. The Local Group is about 3 million light years across with the two large spirals, The Milky Way and Andromeda Galaxy, dominating the two ends. The closest clusters to us are respectively Virgo Cluster, Fornax Cluster, Antlia Cluster, Centaurus Cluster and Hydra Cluster. A galaxy cluster generally contains a central dominant and very luminous elliptical galaxy, namely cD galaxies. Optical luminosity of cD galaxies is typically  $L_B \sim 10^{11} L_\odot$ , which is 10 times higher than our galaxies. %20 of all rich galaxy clusters contain a cD galaxy that also can be seen in faint and poor clusters.

The spatial distribution of member galaxies in clusters is empirically represented by King model [4]:

$$N = N_0 \left[ 1 + \left( \frac{R}{R_c} \right) \right]^{-\frac{3}{2}}$$

Where  $R$  is the three-dimensional radius from the cluster center,  $R_c$  is core radius and  $N_0$  is the central galaxy density. This model gives an approximate solution for particle distribution in a self-gravitating hydrostatic isothermal system.

Bahcall [5] suggested that a formula of form:

$$N = N_0 \left[ 1 + \left( \frac{R}{R_c} \right) \right]^{-\frac{3}{2} \times 0.8}$$

According to Bahcall's study this model represents galaxy distributions better than King model [4].

The luminosity function of galaxies in a cluster is well reproduced by Schechter function [6]:

$$n(L) dL = N^* \left( \frac{L}{L^*} \right)^{-\alpha} * \exp\left(-\frac{L}{L^*}\right) d\left(\frac{L}{L^*}\right)$$

Where  $L^*$  is a characteristic luminosity with typical value of  $10^{10.676} L_\odot$  and  $\alpha$  is typically 1.25. Luminosity function of faint galaxies is not well represented by Schechter function.

#### 1.1.4 Intra-Cluster Medium

Intra-cluster medium is superheated plasma present at the center of a galaxy cluster. Temperature of ICM varies between  $10^7 - 10^8$  K and an atomic density  $\leq 10^{-3} \text{cm}^{-3}$  ICM contains mainly ionized hydrogen and helium and most of baryonic material in the cluster. It emits luminous X-ray radiation where  $L_x \sim 10^{43} - 10^{45} \text{erg/s}$ .

As the ICM in the core of many galaxy clusters is dense, it emits a lot of X-ray radiation. In the absence of heating, the ICM should be cooling. As it cools, hotter gas will flow in to replace it. This is known as cooling flow. The radiative cooling time of a gas which, emits x-rays is roughly:

$$t_{cool} \propto \frac{T_x^{1/2}}{\rho_g}$$

Where  $T_x$  is thermal bremsstrahlung,  $t_{cool}$  is radiative cooling time and  $\rho_g$  is gas density.

Another emission from ICM is the line emission from heavy elements, such as O, Ne, Mg, Si, S and Fe. These metals ejected from member galaxies. The quantity of metals in the ICM is represented by the relative abundance or equivalent width (EW).

In hydrostatic equilibrium with assumption of spherical symmetry, the gas density, temperature and pressure are related to the mass by:

$$\frac{dP_g}{dr} = \frac{\rho_g GM(<r)}{r^2} \quad P_g = \frac{\rho_g k T_x}{\mu m_p}$$

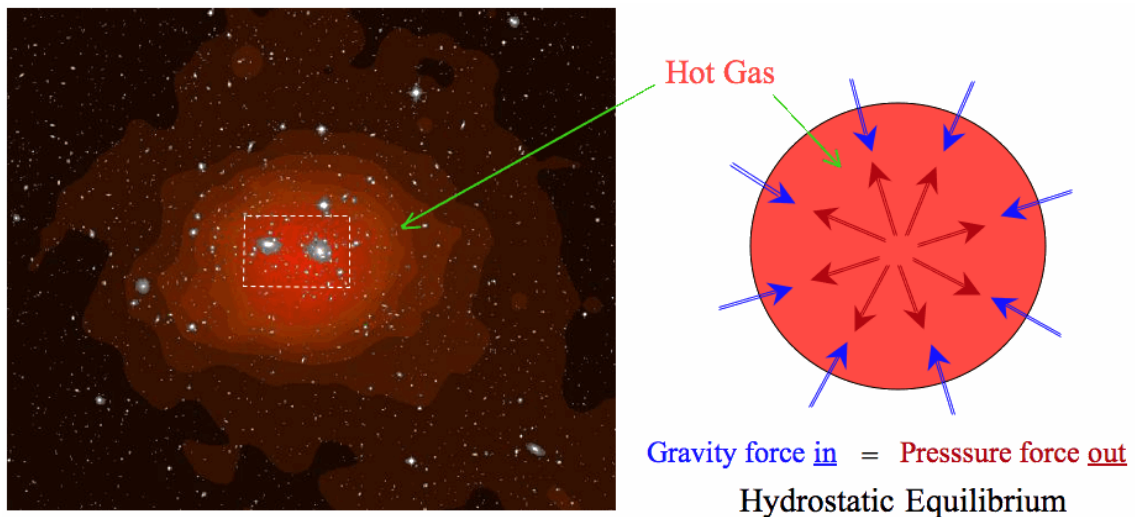


Figure 1.1 Coma Cluster, X-ray (Red) Optic (White)  
Figure 1.2 Hydrostatic Equilibrium of a Spherical Object

## 1.2 Objective of the Thesis

The main aim to compare X-ray point source densities between clusters and non-clusters fields. Since point like emission within clusters can explain with low mass X-ray binaries, active galactic nuclei and halo, systematic studies can provide many useful informations about the nature of X-ray sources within galaxy clusters.

The second objective is to study properties of clusters of galaxies, Abell 3581( $z=0.023$ ) and Abell 400 ( $z=0.0244$ ).

### 1.3 Hypothesis

X-Ray study of point sources within clusters is a challenge cause of very luminous emissions from Intra-Clusters Medium and limited resolution of X-ray telescopes. Nevertheless, thanks to high-resolution cameras of XMM Newton and multi band source detection It is now possible to study X-ray point sources within clusters, yet choosing clusters with faint ICM would be smart way to study point sources.

Several redshifts clusters of galaxies the relative fraction of active galaxies in rich clusters was considerably lower than in the field [7],[8]. Traditional optical studies overlook these sources and arrive at a fraction of 1% of all cluster galaxies harboring an AGN [8]. Including these X-ray–selected AGNs, however, yields a fraction of 5%, consistent with the fraction of field galaxies hosting an AGN on the basis of optical studies [9]. X-ray–selected AGN fraction in clusters is much higher than the optically selected AGN fraction [10]. Then AGN populations in low redshift clusters ( $0.05 \leq z \leq 0.31$ ) have been confirmed [11]. While Montero-Dorta [12] reports a decline in the fraction of low-luminosity AGNs toward the centers of low-redshift clusters; they find an increase in the fraction of LINERs in higher density environments. The difference is likely a result of evolution. [12]

At low redshifts, due to low luminosity AGN associated with cluster excess emission and population seems to be large. One of the early studies by [13] with ROSAT for A2256 ( $z=0.06$ ) found twice as many sources than were expected from blank field.

## CHAPTER 2

---

### XMM-NEWTON

The 4 tonne, 10 m long XMM-Newton spacecraft is the largest scientific satellite ever launched by the European Space Agency. Artist's impressions of XMM-Newton in orbit are shown below as a first overview of the satellite.

#### 2.1 Spacecraft

##### 2.1.1 Components

- The Focal Plane Assembly (FPA), consisting of the Focal Plane Platform (FPP) carrying the focal-plane instruments: two Reflection Grating Spectrometer (RGS) readout cameras, an EPIC PN and two EPIC MOS imaging detectors, and the data handling and power distribution units for the cameras.
- The Telescope Tube (a long carbon fibre tube), maintaining the relative position between the FPA and the MSP. Due to its length of 6.80 m, the Telescope Tube is physically composed of two halves: the upper and lower tubes
- The Mirror Support Platform (MSP), consisting of the platform itself and carrying the three mirrors assemblies (Mirror Modules + entrance and exit baffles + doors + two RGS grating boxes), the Optical Monitor (OM) and the two star-trackers.
- The Service Module (SVM), which carries the spacecraft subsystems and associated units providing the necessary resources to the satellite. Also attached to the SVM are the two solar-array wings, the Telescope Sun Shield (TSS) and the two S-band antennas mounted on their booms.

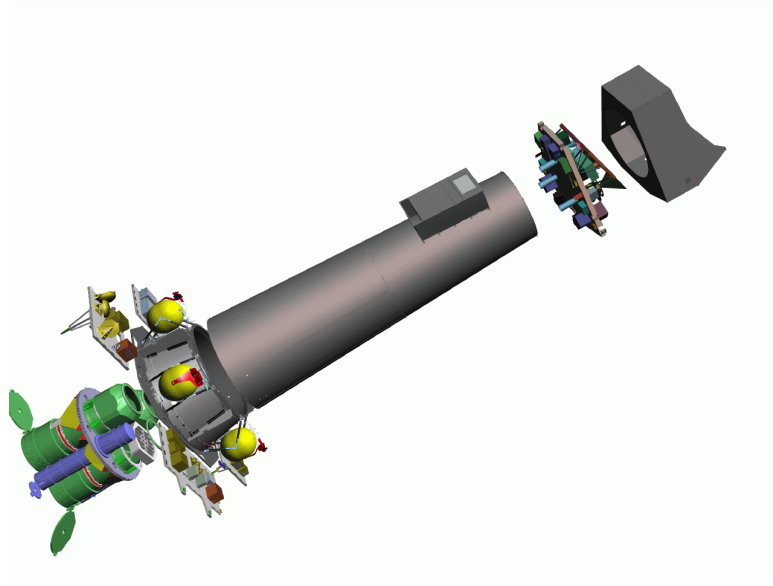


Figure 2.1 The X-ray telescopes are visible at the lower left, as well as the (blue) OM telescope.

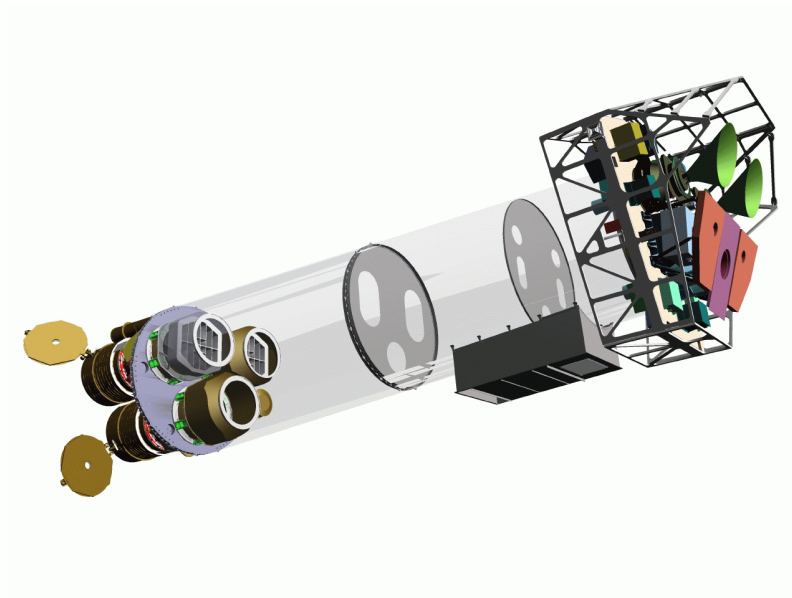


Figure 2.2 the XMM spacecraft were made of glass, one could gain the above view of its payload.

### **2.1.2 Structural Design**

The spacecraft structure, like any other structure, is there primarily to guarantee the integrity of the spacecraft under any loading, such as during handling, testing and launch. In addition, it must allow the spacecraft to serve as an optical bench for a telescope and therefore the structure must provide the necessary thermo-elastic stability in orbit. In the case of XMM-Newton, this led immediately to the selection of ultra-high-modulus carbon-fibre composites (low thermal expansion) for the main structural elements. Another advantage of this material is its very high modulus of elasticity, which limits structural mass for a structure like this, which is designed for stiffness.

These two favourable qualities of this carbon-fibre material, plus its low mass, have led to its widespread use on XMM, albeit for different reasons in different parts. For instance, for the telescope tube and the mirror support platform, a carbon-fibre composite was necessary for thermo-elastic reasons.

In complex items, such as the mirror support platform, the joints that are necessarily made out of metal degraded the intended high thermo-elastic stability to such a level that active thermal control was necessary. Here, a carbon-fibre composite was selected for its high stiffness and strength. Other parts outside the optical path were made of aluminium for reasons of thermal conductivity light-tightness and ease of production.

### **2.1.3 Thermal constraints**

The mirror shells of the Mirror Modules have to be kept at an average temperature of 20°C, with spatial maximum temperature differences of  $\pm 2^\circ\text{C}$  in order to limit thermo-elastic deformations. Therefore, the platform is maintained almost isothermal, with deviations of less than  $\pm 2^\circ\text{C}$ . The thermal design of XMM takes the full advantage of the stable environment provided by its high-altitude, long-period orbit and by the limited variation of solar attitude angles ( $\pm 20^\circ$  pitch combined with  $\pm 20^\circ$  roll). In fact, the Earth albedo and infrared heat fluxes are negligible along the largest part of its high-altitude orbit. The largest thermal perturbations occur during the eclipse seasons, when the satellite does not receive the Sun's energy for a maximum period of 1.7 h. However, eclipses always occur below the minimum altitude that is required for observation (40 000 km), leaving time for the spacecraft to recover its temperature stability.

## **2.2 Mirrors**

### **2.2.1 Introduction**

Each of the three X-ray telescopes on board XMM-Newton consists of 58 Wolter I grazing-incidence mirrors that are nested in a coaxial and confocal configuration. The design of the optics was driven by the requirement of obtaining the highest possible effective area over a wide range of energies, with particular emphasis in the region around 7 keV. Thus, the mirror system had to utilize a very shallow grazing angle of 30' in order to provide sufficient reflectivity at high energies. The telescopes focal length is 7.5 meters and the diameter of the largest mirrors is 70 cm, to be compatible with the shroud of the launcher.

### **2.2.2 Telescope Configuration**

Each of the XMM-Newton telescopes consists of:

- The mirror assembly door, which protected the optics during integration, launch and early orbit phase,
- The entrance baffle, which provides visible straylight suppression at angles larger than 47°,
- The X-ray baffle,
- The Mirror Module,
- An electron deflector, which produces a circumferential magnetic field which prevents low energy electrons reflected by the mirrors reaching the focal plane detectors,
- In two of the telescopes, the Reflection Grating Array, and
- The exit baffle, which provides an appropriate thermal environment.

X-ray baffles are located in front of the mirror systems. They act as collimators and reduce considerably the amount of straylight in the field of view cameras. The XMM-Newton X-ray baffle was constructed as two sieve-plates made out of circular strips. The plates were mounted coaxial to and coaligned with the front aperture cross section of the 58 mirror shells, such that they block single-reflection rays, but do not eclipse two-reflection rays. Each sieve plate is a disk 1 mm thick

with 59 circular strips and 16 radial spokes. The offset of the two sieve plates from the front of the mirror system is 385 mm and 439 mm, respectively. All the baffle surfaces facing the mirrors are blackened.

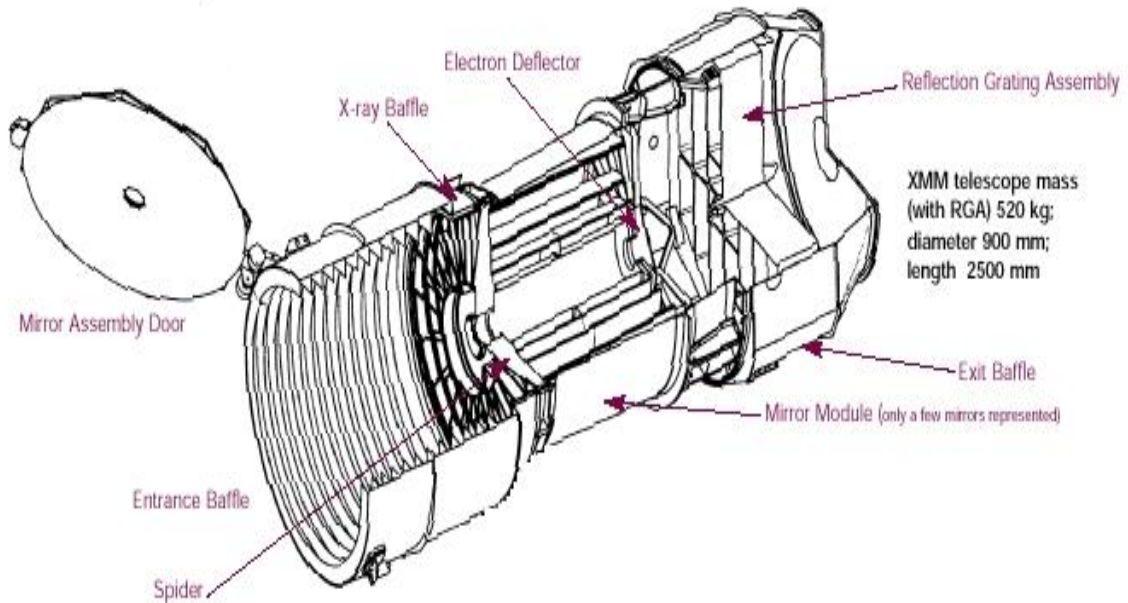


Figure 2.3 The 58 Wolter I mirrors of each telescope are bonded on their entrance aperture to the 16 spokes of a single spider made out of Inconel. The spider is connected to the support platform via an aluminium interface structure (the MIS: Mirror Interface Structure) consisting of an outer cylinder and an interface ring. On two of the modules, the ring interfaces the mirror module to a Reflection Grating Assembly (RGA).

### 2.2.3 Optical Design

Each Mirror Module is a grazing-incidence Wolter I telescope, consisting of 58 gold-coated nested mirrors. Each mirror shell consists of a paraboloid and an associated hyperboloid, which were replicated, together in one piece to facilitate alignment and integration.

In grazing incidence optics the effective area is increased by nesting a number of mirrors and thus filling the front aperture as far as possible. The nesting efficiency is determined by the mirror shell thickness and, in case of very low grazing angles, by the minimum radial mirror separation, which is required for integration and alignment. The thinner the mirror shells are and the narrower the shells are spaced, the larger is the collecting area.

The thickness of the smallest mirror (diameter=306 mm) is 0.47 mm, and it increases linearly with shell diameter in order to guarantee sufficient stiffness. The thickness of the 700 mm diameter mirror is 1.07 mm. The minimum radial separation between adjacent shells is 1mm. Adding more shells is rather inefficient in building up more collecting area because of the mass penalty involved and the low gain in effective area.

#### **2.2.4 Image Quality**

The point spread functions and effective areas of the three telescopes were first characterized on-ground during an extensive calibration campaign. A comprehensive numerical model of the mirror system was used to generate an initial calibration database by extrapolating on-ground tests to in-orbit operation conditions and by interpolating between the finite number of measurement points.

On January 19 2000, the X-ray telescope FM2 saw "First Light", followed by FM3 and FM4. After "First Light" a number of observations were made during the commissioning phase in order to characterize the imaging performance of the telescopes. Analysis of the results indicated that the telescopes point responses measured in-orbit were basically the same as derived from on-ground calibration measurements out to 30". In particular, extended sources in the center of the telescope field of view can be studied with a 5" spatial resolution.

For on-axis sources, high energy photons are focused predominantly by the inner shells of the telescope. These inner shells apparently give better focus than the average hence the fractional encircled energy increases with increasing photon energy.

#### **2.2.5 Effective Area**

The design driver was to achieve maximal area at low energies (2 keV) without sacrificing area at high energies (7 keV). XMM mirrors are most efficient in the energy range from 0.1 to 10 keV, with a maximum around 1.5 keV and a pronounced edge near 2 keV. The design goal was to achieve a collecting area of 1900 cm<sup>2</sup> for energies up to 150 eV, 1500 cm<sup>2</sup> at 2 keV, 900 cm<sup>2</sup> at 7 keV, and 350 cm<sup>2</sup> at 10 keV, for each of the telescopes.

### **2.2.6 X-ray Straylight Rejection**

X-rays from outside the field of view can reach the sensitive area of the focal plane detectors by single reflection from the rear end of the hyperbola, if the source is at an off-axis angle between 20' and 80'. Rays reflected just once from any one of the parabolas can't leave the mirror assembly because of the close packing of the mirror shells. The efficiency of the sieve plate system was ray traced and demonstrated to reduce the straylight level by a factor of 5 to 10 depending on the position in the focal plane. Pointings in the vicinity of the Crab Nebula confirmed the high efficiency of the baffles. The straylight collecting area of the EPIC detectors as a function of off-axis angle is about 3 cm<sup>2</sup> for sources located between 20' and 1.4° from the optical axis, and completely negligible at higher angles.

## **2.3 EPIC**

### **2.3.1 Introduction**

XMM-Newton spacecraft is carrying a set of three X-ray CCD cameras, comprising the European Photon Imaging Camera (EPIC). Two of the cameras are MOS (Metal Oxide Semi-conductor) CCD arrays. The third X-ray telescope has an unobstructed beam; the EPIC instrument at the focus of this telescope uses pn CCDs and is referred to as the pn camera.

The EPIC cameras offer the possibility to perform extremely sensitive imaging observations over the telescope's field of view (FOV) of 30 arcmin and in the energy range from 0.15 to 15 keV with moderate spectral ( $E/\Delta E \sim 20-50$ ) and angular resolution (PSF, 6 arcsec FWHM).

All EPIC CCDs operate in photon counting mode with a fixed, mode dependent frame read-out frequency, producing event lists, i.e. tables with one entry line per received event, listing (among others) attributes of the events such as the position at which they were registered, their arrival time and their energies. The two types of EPIC, however, differ in some major aspects. This does not only hold for the geometry of the CCD arrays and the instrument design but also for other properties, like e.g., their readout times.

### 2.3.2 Chip Geometry

The MOS EEV CCD22 is a three-phase frame transfer device on high resistivity epitaxial silicon with an open-electrode structure; it has a useful quantum efficiency in the energy range 0.2 to 10 keV. The low energy response of the conventional front illuminated CCD is poor below  $\sim 700$  eV because of absorption in the electrode structure. For EPIC MOS, one of the three electrodes has been enlarged to occupy a greater fraction of each pixel, and holes have been etched through this enlarged electrode to the gate oxide. This gives an "open" fraction of the total pixel area of 40%; this region has a high transmission for very soft X-rays that would otherwise be absorbed in the electrodes. In the etched areas, the surface potential is pinned to the substrate potential by means of "pinning implant". High energy efficiency is defined by the resistivity of the epitaxial silicon (around 400 Ohm-cm). The epitaxial layer is 80 microns thick (p-type). The actual mean depletion of the flight CCDs is between 35 to 40 microns: the open phase region is not fully depleted.

The schematic view looking into the pn-CCD introduces intuitively the advantages of the concept: X-rays hit the detector from the rear side. In the event of an X-ray interaction with the silicon atoms, electrons and holes are generated in numbers proportional to the energy of the incident photon. The average energy required to form an electron-hole pair is 3.7 eV at  $-90^\circ$  C. The strong electric fields in the pn-CCD detector separate the electrons and holes before they recombine. Signal charges (in our case electrons), are drifted to the potential minimum and stored under the transfer registers. The positively charged holes move to the negatively biased back side, where they are 'absorbed'. The electrons, captured in the potential wells 10 microns below the surface can be transferred towards the readout nodes upon command, conserving the local charge distribution patterns from the ionization process. Each CCD line is terminated by a readout amplifier.

## Comparison of focal plane organisation of EPIC MOS and pn cameras

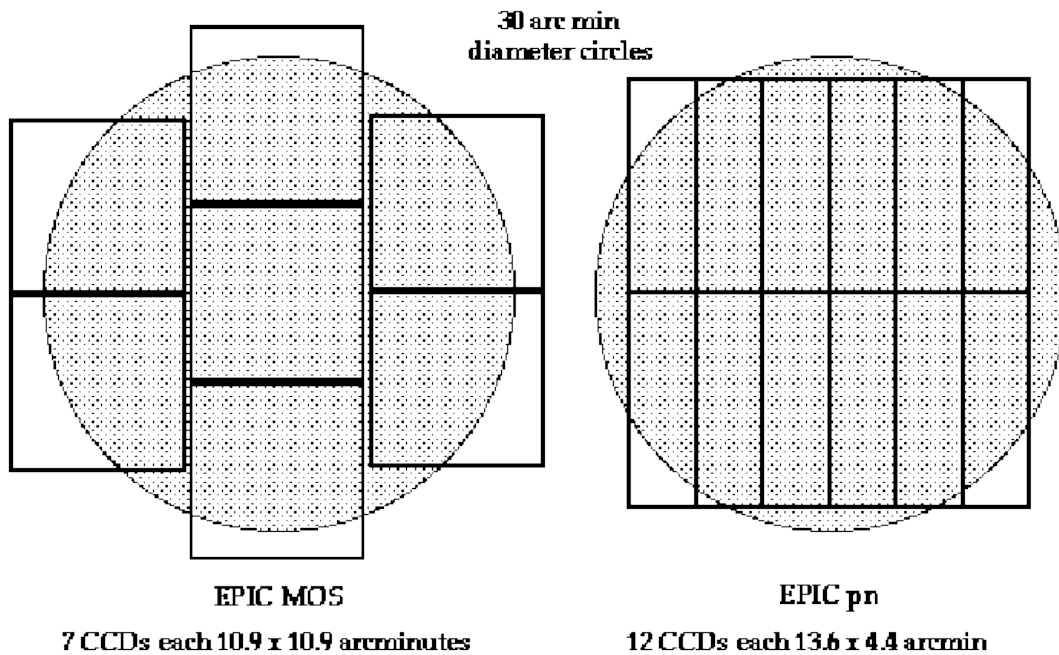


Figure 2.4 A rough sketch of the field of view of the two types of EPIC camera; MOS (left) and PN(right). The shaded circle depicts a diameter area.

### 2.3.3 Operating Modes

The EPIC cameras allow several modes of data acquisition. Note that in the case of MOS the outer ring of 6 CCDs remain in standard full-frame imaging mode while the central MOS CCD can be operated separately. The pn camera CCDs can be operated in common modes in all quadrants for full frame, extended full frame and large window mode, or just with one single CCD (CCD0 in quadrant 1) for small window, timing and burst mode.

- Full frame and extended full frame (pn only)

In this mode, all pixels of all CCDs are read out and thus the full FoV is covered.

- Partial window

a) MOS: In a partial window mode the central CCD of both MOS cameras can be operated in a different mode reading out only part of the CCD chip: in **small window** mode an area of 100 x 100 pixels is read out, whereas in **large window** mode an area of 300 x 300 pixels is active.

b)pn: In **large window** mode only half the area of all 12 CCDs is read out, whereas in **small window** mode only the part of CCD0 in quadrant 1 at the focal point is used to collect data

### 2.3.4 Instrument Characteristics

One of the factors to be taken into account when determining the effective area of the EPIC cameras is their quantum efficiency. It is the quantum efficiency of the EPIC-MOS chips that limits the energy passband at its high energy end, while the pn camera can detect photons with high efficiency up to 15 keV.

The EPIC background can be divided into two parts: a cosmic X-ray background (CXB), and an instrumental background. The latter component may be further divided into a detector noise component, which becomes important at low energies (below 200 eV) and a second component, which is due to the interaction of particles with the structure surrounding the detectors and the detectors themselves. This component is characterized by a flat spectrum and is particularly important at high energies (above a few keV). The particle induced background can be divided into two components: an external 'flaring' component, characterized by strong and rapid variability, which is often totally absent and a second more stable internal component. The flaring component is currently attributed to soft protons (with energies smaller than a few 100 keV), which are funneled towards the detectors by the X-ray mirrors. The stable component is due to the interaction of high-energy particles (with energies larger than some 100 MeV) with the structure surrounding the detectors and possibly the detectors themselves.

There are four filters in each EPIC camera. Two are thin filters made of 1600 Å of polyimide film with 400 Å of aluminium evaporated on to one side; one is the medium filter made of the same material but with 800 Å of aluminium deposited on it; and one is the thick filter. This is made of 3300 Å thick Polypropylene with 1100 Å of aluminium and 450 Å of tin evaporated on the film. The filters are self-supporting and 76 mm in diameter. The remaining two positions on the filter wheel are occupied by the closed (1.05 mm of aluminium) and open positions, respectively. The former is used to protect the CCDs from soft protons in orbit, while the open position could in principle be used for observations where the light flux is very low, and no filter is needed.

### OBSERVATION AND DATA REDUCTION

#### 3.1 Motivations and Source Selection

In order to compare X-ray sources within cluster with field sources, we have selected two low redshift clusters. Studying point like sources is quite difficult. While selecting sources to study, we adopted a few important facts. First of all, we selected clusters that do not have bright ICM emission, so disclosing point-like sources became possible. Secondly, inspecting central region of nearby cluster is statistically more reliable than distant ones. Lastly, having close temperatures, because temperature differences trigger indistinct effects.

In this study, we present X-ray point sources observed in the field of two nearby clusters A3581 ( $z=0.023$ ) and A400. ( $z=0.0244$ ). Luminosity value of A3581 and A400 is  $0.6 \times 10^{44}$  [14] and  $0.4 \times 10^{44}$  [15]. Abell 3581 has a cd galaxy (IC 4374) that is a strong radio source and has brighter ICM than Abell 400. Its ICM temperature is 2.0 keV [16]. Abell 400 dominated by pair of giant ellipticals (NGC 1128) that also are radio jets. NGC 1128 contains two supermassive black holes spiraling towards merger (3C 75) and its ICM temperature is 2.48 keV [16].

We adopt deceleration parameter  $q_0= 0.55$  and Hubble Constant  $H_0= 70 \text{ km s}^{-1} \text{ Mpc}^{-1}$  [17] with a resulting luminosity distance 103 Mpc for A400 and 104 Mpc for A3581 and angular size of 1 arc min corresponds to 28.71 kpc and 28.89 kpc respectively.

### **3.2 Observation**

We use X-ray data obtained by XMM-Newton satellite that cover almost entire cluster region (~30 arcmin). The European Photon Imaging Camera (EPIC) has two MOS and a PN detector.

Abell 400 was observed with XMM-Newton for 38.9ks on 2006 August 06 (OBSID 0404010101) and A3581 was observed on 2007 August 01 for 117.1ks(OBS ID 0504780301) The EPIC MOS-1, MOS-2 and PN cameras were operated with thin filters in Prime Full Window mode for A400 and with medium filter in Prime Full Window mode for A3581.

### **3.3 Data Reduction**

We generated event list by using EPCHAIN and EMCHAIN tasks from the Observation Data File. To outcome flaring particle background, we clipped light curve for MOS ( $>10\text{keV}$ ) and PN ( $>10\text{keV}$ ,  $<12\text{keV}$ ) where rate expression is  $\text{RATE} \leq 0.35$  for EPIC-MOS and  $\text{RATE} \leq 0.40$  for EPIC-PN. Finally, Good Time Intervals selection applied to event list to produce filtered event file. Data were filtered using patterns corresponding single and double pixel events for PN (0-4) and single quadruple events for MOS (0-12), together with the flags #XMMEA\_EM (MOS) and #XMMEA\_EP (PN) to remove hot pixels and out of field events.

### **3.4 Background Selection**

The background photons in principle can be selected within a ring around the source. We selected 45 arc-sec radius that covers %90 of fractional energy of encircled energy function (EEF). Background counts were extracted from source counts. We used 'BACKSCALE' command to exclude ccd-gaps and bad-pixels within selected sources.

#### 4.1 Overview

##### 4.1.1 Abell 3581

Abell 3581 ( $z=0.023$ ) is X-ray bright cluster of galaxies with richness class 0 and Bautz Morgan Type I according to its morphology. There is a strong radio source (PKS-1404-267) that associated with central dominant galaxy that also has extensive optical emission (IC 4374) [18]. Its luminosity distance is 104 arcmin where 1 arcmin corresponds to 28.98 kpc. Abell 3581 has a cool Intra-cluster medium with  $kT \sim 2$  keV [18].

##### 4.1.2 Abell 400

Abell 400 ( $z=0.0244$ ) is faint clusters of galaxies with richness class I and Bautz Morgan Type II-III. Abell 400 contains the galaxy pair (NGC 1128) at the center of cluster with 2 supermassive black holes (3C 75) spiraling towards merger. Also there are strong radio jets at the center that are also known as (3C75). 3C 75 is a bound system that is rapidly losing energy and actual separation of black holes is  $\sim 8$  kpc [19]. Its luminosity distance is 103 Mpc where 1 arcmin corresponds to 28.71 kpc. Abell 400 also has cool ICM with  $kT \sim 2.48$  keV [16].

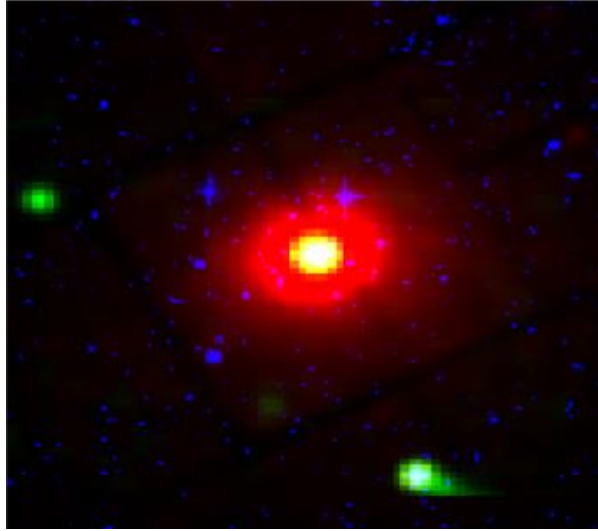


Figure 4.1 True color image of Abell 3581. (Green=Radio Red=X-ray Blue=Optic)

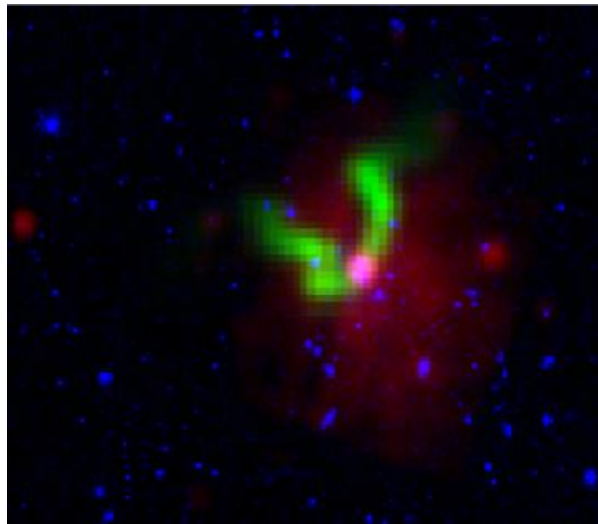


Figure 4.2 True color image of Abell 400. (Green=Radio Red=X-ray Blue=Optic)

## 4.2 X-ray Images

The X-ray appearance of a galaxy cluster gives much useful information about cluster structure. A detailed knowledge on the cluster structure may lead us to understand the formation of the universe. With that motivation, we created X-ray images for our cluster samples with 3 different energy bands by using events file that shows how many photons hit each pixel of the detector. We selected energy bands as soft, medium and hard. Also we created all band images of our samples. The broad band is 0.2-12 keV, soft band is 0.3-1.0 keV, medium band is 1-1.6 keV and hard band 1.6-10 keV. The images below display MOS and PN images separately in soft, medium, hard and broad band for both our clusters.

### 4.2.1 A3581 ICM Shape

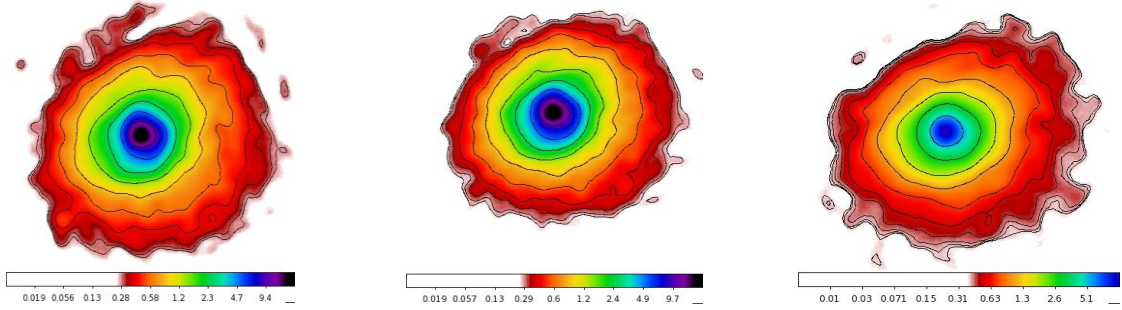


Figure 4.3 MOS1 ICM image of Abell 3581 in three energy band, respectively soft, medium and hard images

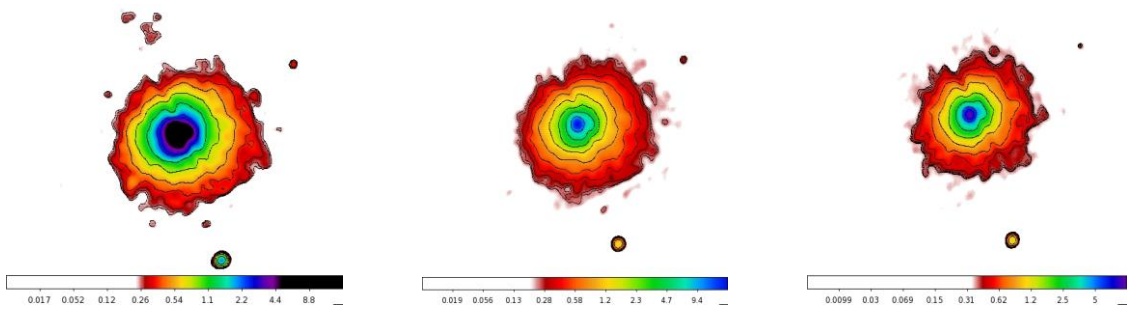


Figure 4.4 MOS2 ICM image of Abell 3581 in three energy band, respectively soft, medium and hard images

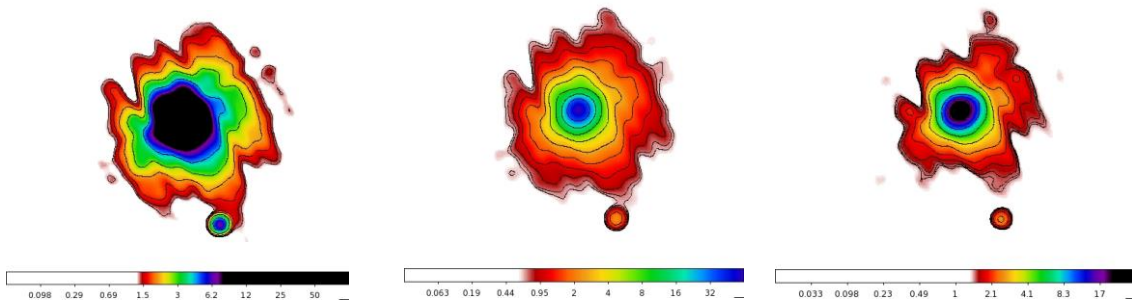


Figure 4.5 PN ICM image of Abell 3581 in three energy band, respectively soft, medium and hard images

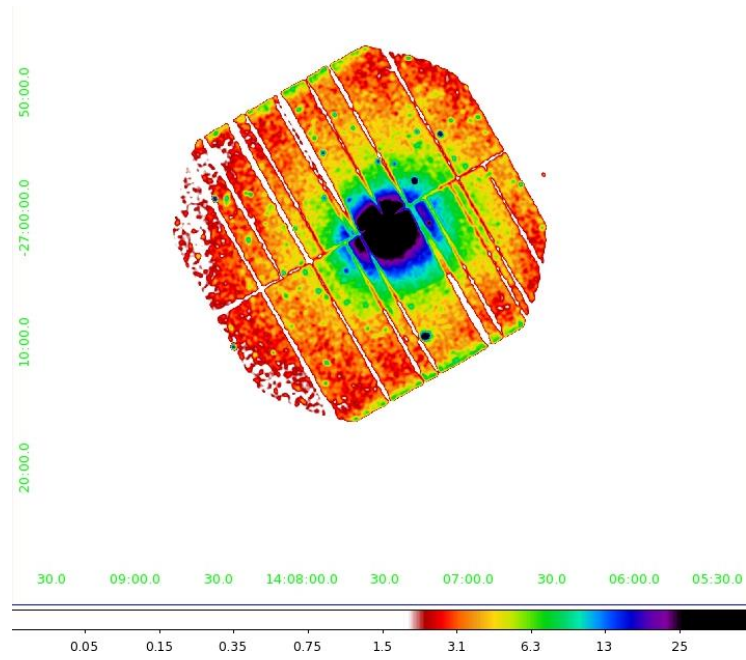


Figure 4.6 Mosaic image of Abell 3581 in broad energy band

#### 4.2.2 A400 ICM Shape

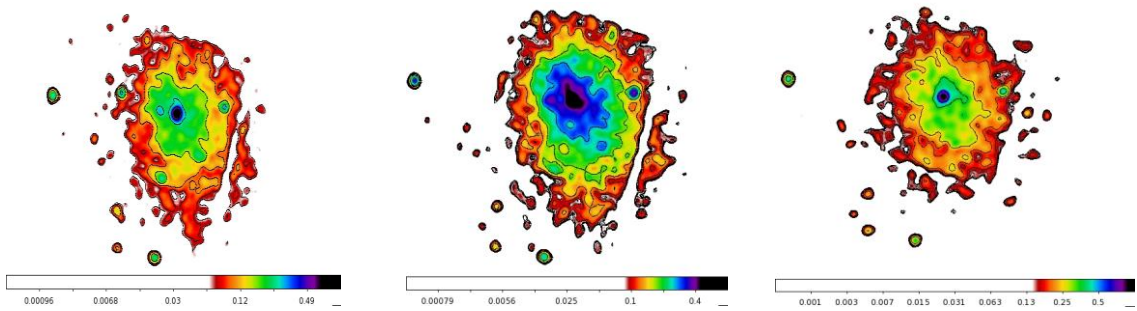


Figure 4.7 MOS1 ICM image of Abell 400 in three energy band, respectively soft, medium and hard images

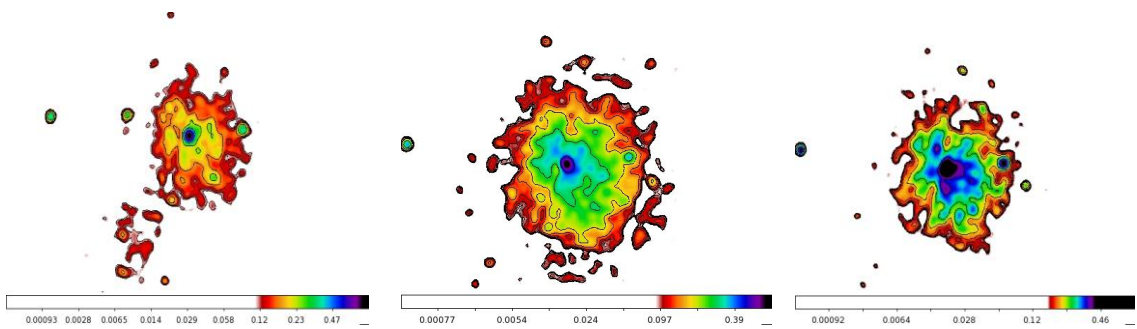


Figure 4.8 MOS2 ICM image of Abell 400 in three energy band, respectively soft, medium and hard images

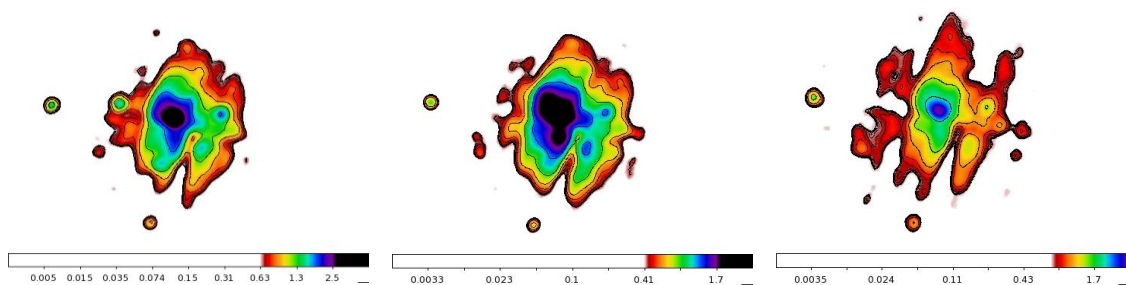


Figure 4.9 PN ICM image of Abell 400 in three energy band, respectively soft, medium and hard images

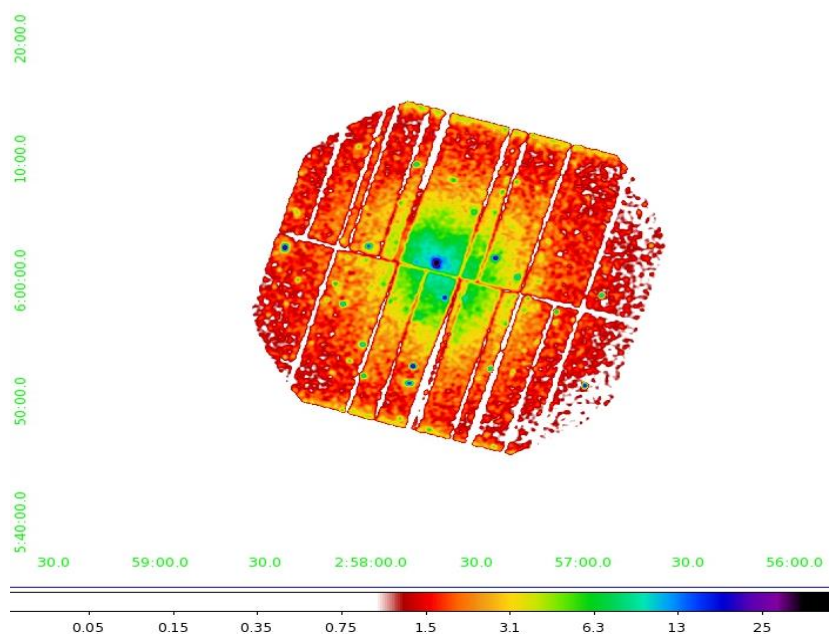


Figure 4.10 Mosaic image of Abell 3581 in broad energy band

### 4.3 Source detections

We applied The SAS source detection algorithms to the data. Source detection is performed with SAS Task, namely “EDEDTECT\_CHAIN”. We used 3 different EPIC Images in the soft band of “0.3-1.0 keV”, in the medium band of “1.0-1.6 keV” and in the hard band of “1.6-10 keV to for source detection. Source detections were accepted with likelihood values above 10 (about  $4\sigma$ ) and inside an off-axis angle of 13 arcmin. We selected minimum likelihood  $ml=10$  and a  $4\sigma$  Gaussian of the signal-to-noise ratio. The raw source count rates have been converted to X-ray fluxes by applying a correction for vignetting and dead time plus out of time events as well as the counts-to-

flux conversion factor (ECF). Energy Conversion Factor has been calculated by considering their filter type and column density and also with assumption of  $\Gamma = 1.7$ . Detection routine has been applied for both MOS and PN cameras and the final list has been prepared with SAS task “SRCMATCH”. Sources falling outside 12.5 arcmin radius and sources at CCD gaps were removed.

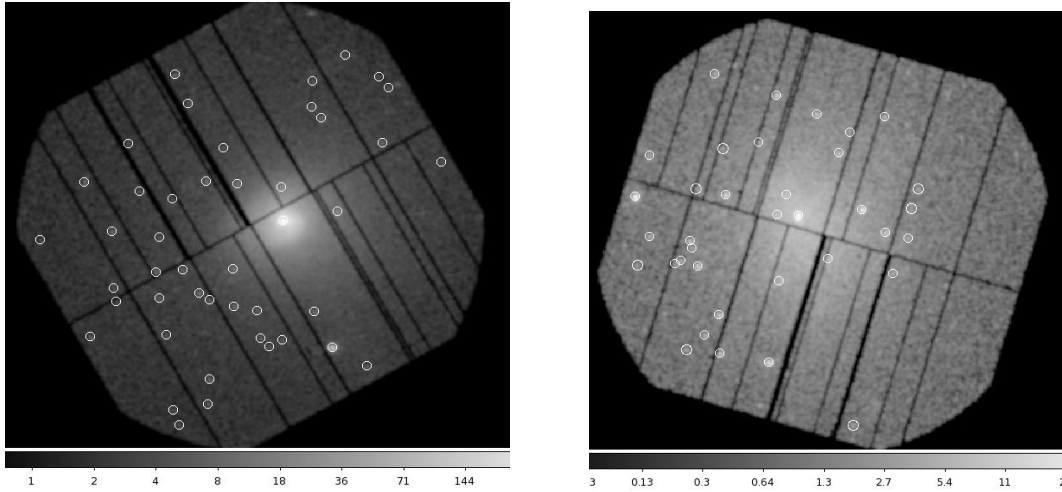


Figure 4.11 Detected Sources of Abell 3581 and Abell 400 respectively.

#### 4.4 $\log(N) - \log(S)$

##### 4.4.1 Solid angle of the survey

The characteristic of solid angle is the same as that for clusters and field; survey area decreases with flux. Because of that, it was necessary to understand limiting flux for our observations. We calculated limiting flux of our survey by multiplying Energy Conversion Factor sensitivity map image. Energy conversion factor was calculated by considering camera’s filter and by using  $\Gamma = 1.7$  photon index assumptions.

In addition, galactic absorption column values of our clusters were considered while calculating ECF. We calculated average energy conversion factor by using spectral models. According to our computations, ECF value of A3581 is  $2.86 \times 10^{-12}$  and ECF value of A400 is  $3.11 \times 10^{-12}$ . Solid angle of our clusters shows that flux value  $< 10^{-14} \text{cm}^{-2} \text{s}^{-1}$  need to be corrected.

#### 4.4.2 Cumulative source number per degree square

Cumulative source number per degree square can be calculated as function of flux with equation below:

$$N(> S) = \left( \sum_{i=1}^n \frac{1}{\Omega_i} \text{deg}^{-2} \right)$$

Where n is the detected source number,  $\Omega_i$  = sky coverage for the flux of the i -th source. Figure ‘’ shows Log (N) – Log (S) relations for A3581 and A400 and Lockman Hole results measured by Hasinger [20]. Hard energy band is much susceptible to cosmic variance than soft energy band. We used 2-10keV fluxes at our Log N – Log S calculations.

## CHAPTER 5

---

### RESULTS AND DISCUSSION

We analyzed XMM Newton observation of Abell 3581 and Abell 400. 34 sources are detected for Abell 3581 and 32 sources detected for Abell 400. We used cumulative source number per degree square method to calculate LogN - LogS plot. According to Log N - Log S plot, our source density values correspond to  $346 \pm 67$  sources  $\text{deg}^{-2}$  for Abell 3581  $372 \pm 72$  sources  $\text{deg}^{-2}$  for Abell 400 around logarithmic flux limit of 13.9. At this flux level, density of  $199 \pm 30$  sources  $\text{deg}^{-2}$  from Lockman Hole are calculated by Hasinger [20]. If we use minimum possible source density level for our samples and maximum source density of Lockman hole, excess emission from clusters can be seen. A comparison of the cluster source density with both non-cluster fields implies an elevated AGN activity in the cluster environment. Close encounters and possible collisions of galaxies are highly possible in cluster environments. When a galaxy fall into cluster environments under the influence of gravitational potential, surrounding gas powers AGN, therefore, the source becomes brighter. In addition, Most of galaxies host an Black hole at its center. Most of them are inactive. Possible ICM fuelling may activate the inactive Black Hole, which increases X-ray source density in clusters.

To explain origin of X-ray emission, individual galaxies are studied. X-ray emissions mainly comes from central AGN, discrete sources and diffuse galactic gas. Sarazin [23] reports most of X-ray emissions from elliptical galaxies comes from LMXBs. Blanton [24] also reports most of X-ray emissions at lenticular galaxies comes from LMXBs. Clusters are dominated by ellipticals and lenticulars [21]. In order to understand X-ray emission, we focus on two possible cases; LMXBs and LLAGNs.

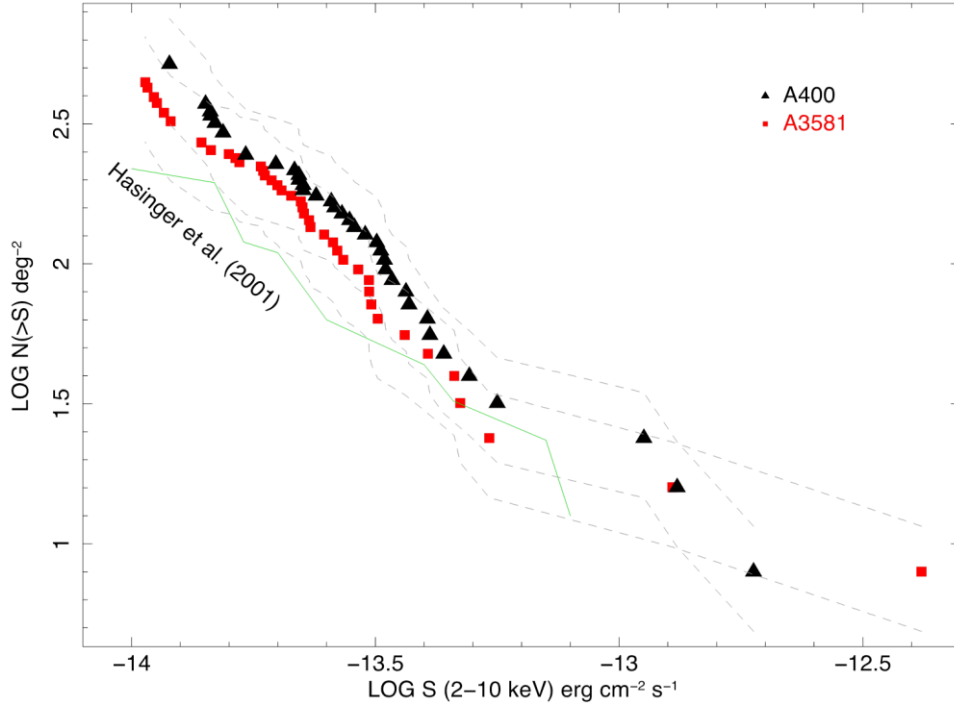


Figure 5.1 Log (N) – Log (S) distributions of the sources from Abell 3581 and Abell 400. Green lines represents average distributions of field sources studied by Hasinger [20]. Dashed lines represents 4 sigma gaussian error.

X-ray to optical luminosity ratio ( $L_x/L_B$ ) are studied. Matsushita [22] studied nature of early type galaxies with  $L_x/L_B$  plot, with this motivation, we compared our  $L_x/L_B$  to explain X-ray emissions of our samples. Optical properties of galaxies are given in Table 5.1. Apparent blue magnitudes were taken from ned archive. Absolute blue magnitudes, MB are calculated from eq.  $MB = m_B + 5 - 5 \log(d)$  and blue luminosity are calculated from eq.  $LB = -0.4(MB - 5.41)$ .

Matsushita [22] studied average distribution of X-ray compact early-type galaxies with %90 confidence limits. Most of individual X-ray sources of our samples obey Matsushita's distribution [22]. Sarazin [23] and Blanton et al. [24] reports that most of X-ray emission from ellipticals and lenticulars comes from LMXBs, by considering Sarazin and Blanton's reports according to our results, X-ray emission nature of our individual galaxies can be explained by unresolved LMXBs.

Table 5.1 Optical Properties of Individual Galaxies

NAME	z	mb	Mb	log L <sub>B</sub> /L <sub>0</sub>	Log L <sub>x</sub>	Log L <sub>x</sub> /L <sub>b</sub>	Type	NOTE	Group
IC 4373	0,021798	11,367	-23,46	11,548	41,667	30,119	SA0	radio source	A3581
ESO 510-G 066	0,024333	12,59	-22,63	11,216	41,242	30,026	S0		A3581
ESO 510-G065	0,025671	13,74	-21,49	10,76	40,567	29,806	Sb		A3581
CGCG 415-040	0,022886	15	-20,37	10,312	40,107	29,795	S0		A400
CGCG 415-046	0,022782	15,4	-19,97	10,152	40,435	30,283	E		A400
NGC 1128 NED1	0,023823	13,18	-21,75	10,864	40,573	29,709	E	radio jet	A400
NGC 1128 NED 2	0,022152	13,16	-22,21	11,048	41,140	30,092	E	radio jet	A400
NGC 1128 (Galaxy pairs)	0,023153	12,38	-22,34	11,1	41,248	30,148	E0	radio jet	A400

CGCG 415-040 has slightly higher  $L_X/L_B$  value that can be explained with contribution from unresolved sources. According to our  $L_X / L_B$  results, CGCG 415 - 046 is the only source that does not obey average distribution of early type galaxies. It has lowest  $L_X / L_B$  result. CGCG 415-046 has either faint LLAGN or there is no active nucleus. The brightest source in our survey is IC 4373, which is cd galaxy of Abell 3581. It is really bright in both X-ray and optic, yet we don't get any peculiarity.

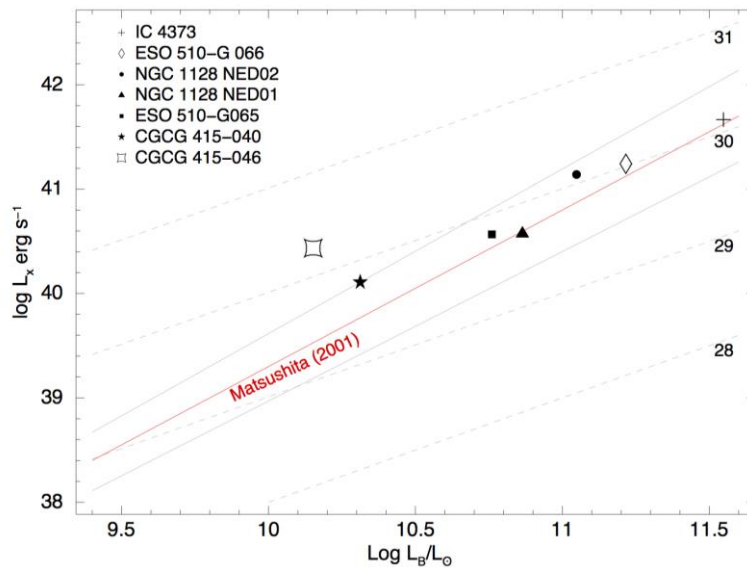


Figure 5.2 Logarithmic  $L_X / L_B$  relation for bright elliptical and spiral galaxies. Red line represents average distribution of early-type galaxies. Grey straight lines indicate %90 confidence limits.

## REFERENCES

---

- [1] Zwicky, F. et al., (1933). “Die Rotverschiebung Van Extragalaktischen Nebeln”, *Helvetica Physica*, 6:110-127
- [2] White, N. E. et al., (1993). “The Formation and Evolution of Galaxies Within Merging Dark Matter Haloes”, *MNRAS*, 264:201
- [3] Abell, G. O., (1961). “Evidence regarding second-order clustering of galaxies and interactions between clusters of galaxies”, *Astronomical Journal*, 66:607A
- [4] King, I. R., (1962). “The Structure of Star Clusters I. An Empirical Density Law”, *The Astronomical Journal*, 67:471
- [5] Bahcall, N. A., (1977). “X-Ray Clusters of Galaxies Corrections With Optical Morphology and Galaxy Density”, *Astrophysical Journal*, 217:L77-L88
- [6] Schechter, P. L., (1976). “An Analytic Expression For Luminosity Function For Galaxies“, *Astrophysical Journal*, 203:297
- [7] Dressler, A. and Gunn, J. E., (1983). “Spectroscopy of galaxies in distant clusters. II - The population of the 3C 295 cluster ”, *APJS*, 294:70
- [8] Dressler, A. et al., (1999). “VizieR Online Data Catalog: Spectroscopic catalog of 10 rich galaxy clusters ”, *APJS*, 122:51
- [9] Barger, A. J. et al., (2002). “X-Ray, Optical and Infrared Imaging and Spectral Properties of the 1 Ms Chandra Deep Field North Sources”, *The Astronomical Journal*, 123:1839
- [10] Martini, P. et al., (2002). “An Unexpectedly High Fraction of Active Galactic Nuclei in Red Cluster Galaxies”, *Astrophysical Journal*, 576:L109
- [11] Martini, P. et al., (2006). “Spectroscopic Confirmation of A Large AGN Population in Clusters of Galaxies”, *Astrophysical Journal*, 644:116M
- [12] Montero-Dorta, et al., (2009). “The DEEP2 Galaxy Redshift Survey: The Red Sequence AGN Fraction and Its Environment and Redshift Dependence”, *MNRAS*, 392:125M
- [13] Henry, J. P. and Briel, U. G., (1991). “The X-ray Morphology of the Relaxed Cluster of Galaxies A2256. II - Sources Around the Extended Cluster Emission”, *Astronomy and Astrophysics*, 246:14H

- [14] De Plaa, J., (2007). “Constraining Supernova Models Using the Hot Gas in Clusters of Galaxies”, *Astronomy and Astrophysics*, 465:345D
- [15] Ebeling, H. et al., (1998). “The ROSAT Brightest Cluster Sample - I. The compilation of the sample and the cluster log N-log S distribution”, *MNRAS*, 301:801
- [16] Frank, K. A. et al., (2013). “Characterization of Intracluster Medium Temperature Distributions of 62 Galaxy Clusters with XMM-Newton”, *APJ*, 764:46F
- [17] Bennett, C. L. et al., (2013). “Nine-year Wilkinson Microwave Anisotropy Probe (WMAP) Observations: Final Maps and Results”, *APJS*, 208:20B
- [18] Johnstone, R. M. et al., (1998). “X-ray and Radio Observations of the Poor Cluster A3581 which Hosts the Radio Galaxy PKS 1404-267”, *MNRAS*, 298:854J
- [19] Yokosawa, M. and Inoue, M., (1985). “Binary galaxy model for wiggling radio jets and its application to 3C 75”, *PASJ*, 37:655Y
- [20] Hasinger, G. et al., (2001). “XMM-Newton observation of the Lockman Hole. I. The X-ray data”, *Astronomy and Astrophysics*, 365L:45H
- [21] Dressler, A., (1980). “A catalog of morphological types in 55 rich clusters of galaxies”, *APJS*, 42:565D
- [22] Matsushita, K., (2001). “Origin of the Scatter in the X-Ray Luminosity of Early-Type Galaxies Observed with ROSAT”, *The Astrophysical Journal*, 547:693M
- [23] Sarazin, C. L. et al., (2001). “Chandra X-Ray Observations of the X-Ray Faint Elliptical Galaxy NGC 4697”, *The Astrophysical Journal*, 556:533S
- [24] Blanton, E. L. et al., (2001). “Diffuse Gas and Low-Mass X-Ray Binaries in the Chandra Observation of the S0 Galaxy NGC 1553”, *Astronomy and Astrophysics*, 556:533S

## APPENDIX-A

### ABELL 3581

In table A.1, analysis results for Abell 3581 are listed. First three columns represents soft, medium, hard energy counts of point sources respectively. Forth column represents logarithmic flux value of selected source in units of  $\text{ergs cm}^{-2} \text{s}^{-1}$ . Fifth column represents logarithmic luminosity value of selected sources in units of  $\text{ergs/s}$ .

Table A.1 Analysis Results for Abell 3581

Src. Name	Soft Counts	Medium Counts	Hard Counts	Flux	Luminosity
XMM J140729.7-270103 (M1)	297,9	220,8	106,7	-12,35	41,74
XMM J140715.6-270931 (S1)	45,91	16,31	12,94	-12,86	41,22
XMM J140827.1-265830 (S2)	2,447	1,363	2,106	-13,27	40,81
XMM J140806.5-270432 (S3)	2,501	0	1,063	-13,64	40,33
XMM J140819.2-270149 (S4)	2,23	1,332	1,022	-13,61	40,47
XMM J140800.9-265123 (S5)	2,762	1,117	1,184	-13,81	40,27
XMM J140751.1-271138 (S6)	2,527	1,203	0	-13,97	40,11
XMM J140714.1-270028 (S7)	4,078	3,418	4,888	-13,35	40,73
XMM J140754.0-270554 (S8)	2,227	1,485	1,176	-13,8	40,28
XMM J140751.8-265829 (S9)	2,497	1,593	2,166	-13,66	40,42
XMM J140730.2-265852 (S10)	13,69	7,538	6,332	-13,35	40,73
XMM J140751.6-271317 (S11)	1,992	0	0	-13,73	40,34
XMM J140743.9-270648 (S12)	2,625	1,71	1,825	-13,59	40,49
XMM J140720.9-270708 (S14)	2,956	0	1,122	-14,37	39,71
XMM J140758.8-270422 (S15)	2,335	1,677	1,348	-13,73	40,35
XMM J140701.2-265554 (S16)	1,103	1,53	2,595	-13,39	40,68
XMM J140718.7-265415 (S17)	2,053	1,511	2,269	-13,6	40,47
XMM J140736.2-270854 (S18)	1,612	0	0	-13,92	40,17

Table A.1 (cont'd)

XMM J140805.5-70615 (S20)	2,18	0	1,43	-13,88	40,2
XMM J140803.6-270840 (S21)	1,118	0	1,399	-13,54	40,42
XMM J140750.8-270621 (S22)	1,374	0	0	-13,97	40,11
XMM J140730.0-270901 (S23)	2,322	0	0	-14,07	39,91
XMM J140818.7-270534 (S24)	1,437	0	0	-13,95	40,15
XMM J140805.5-270211 (S25)	1,105	0	0	-13,97	40,11
XMM J140737.2-270703 (S26)	2,215	1,263	0	-13,93	40,17
XMM J140814.4-265557 (S27)	0	0	1,063	-13,95	40,15
XMM J140811.3-265908 (S28)	0	0	1,544	-13,51	40,47
XMM J140721.3-265140 (S29)	0	0	1,304	-13,63	40,44
XMM J140757.1-265319 (S30)	0	0	1,462	-13,57	40,41
XMM J140747.0-265616 (S31)	0	0	1,621	-13,65	40,42
XMM J140705.5-271045 (B1)	1,48	0	1,146	-13,71	40,36
XMM J140656.9-265159 (B10)	1,683	0	1,152	-13,73	40,35
XMM J140742.9-265838 (Y1)	4,966	2,112	2,63	-13,66	40,42

## APPENDIX-B

### ABELL 400

In table B.1, analysis results for Abell 400 are listed. First three columns represents soft, medium, hard energy counts of point sources respectively. Forth column represents logarithmic flux value of selected source in units of  $\text{ergs cm}^{-2} \text{s}^{-1}$ . Fifth column represents logarithmic luminosity value of selected sources in units of  $\text{ergs/s}$ .

Table B.1 Abell 400 Results

Src. Name	Soft Counts	Medium Counts	Hard Counts	Flux	Luminosity
XMM J025824.6+060248 (S1)	14,32	8,05	13,15	-12,72	41,4
XMM J025741.6+060131 (S2)	32,4	12,24	18,51	-12,88	41,25
XMM J025749.3+055135 (S3)	7,6	5,99	7,13	-12,95	41,18
XMM J025724.7+060156 (S4)	11,11	6,75	7,24	-13,25	40,88
XMM J025808.2+055808 (S6)	4,08	2,97	4,18	-13,37	40,76
XMM J025747.3+060940 (S7)	5,4	2,69	3,59	-13,44	40,69
XMM J025802.3+055448 (S8)	4,93	2,56	2,91	-13,47	40,67
XMM J025802.3+055213 (S9)	3,92	2,13	2,06	-13,67	40,47
XMM J025718.5+060022 (S10)	4,7	3,38	3,82	-13,39	40,74
XMM J025736.7+060822 (S11)	3,79	2,46	2,52	-13,58	40,48
XMM J055730.8+060545 (S12)	3,21	2,62	3,5	-13,44	40,69
XMM J025718.8+060813 (S13)	2,4	1,68	1,96	-13,48	40,65
XMM J025803.6+061107 (S14)	1,76	0	2,15	-13,49	40,64
XMM J025806.2+055327 (S15)	0	0	3,12	-13,31	40,82
XMM J025820.9+060008 (S16)	1,73	0	2,3	-13,65	40,48
XMM J025747.1+060136 (S17)	7,2	5,83	3,58	-13,47	0,66
XMM J025712.5+055964 (S20)	1,07	2,35	2,98	-13,42	40,71
XMM J025733.6+055835 (S21)	5,24	3,92	2,33	-13,43	40,7
XMM J025716.5+055736 (S22)	2,75	2,06	1,47	-13,66	40,47
XMM J025820.9+060537 (S23)	2,7	1,13	2,1	-13,58	40,55
XMM J025752.1+060631 (S24)	1,6	1,08	1,83	-13,52	40,61

Table B.1 (cont'd)

XMM J025810.2+055948 (P1)	1,97	2,22	2,61	-13,51	40,62
XMM J025812.7+055828 (P2)	1,32	1,36	0	-13,92	40,21
XMM J025824.2+055810 (B4)	1,19	0	0	-13,84	40,29
XMM J025709.9+060320 (B7)	0	1,08	1,21	-13,7	40,42
XMM J025711.7+060160 (B9)	1,37	1,72	1,02	-13,77	40,36
XMM J025807.0+060155 (MP2)	1,36	0	1,56	-13,77	40,36
XMM J025801.5+060148 (MP3)	1,78	1,12	1,14	-13,84	40,29
XMM J025702.4+060945 (B6)	1,51	0	0	-13,6	40,58
XMM J025727.0+054721 (B1)	0	0	1,27	-13,65	40,48
XMM J025809.8+055919 (E6)	0	0	0	-13,9	40,22

## CURRICULUM VITAE

---

### PERSONAL INFORMATION

**Name Surname** : Turgay ÇAĞLAR  
**Date of birth and place** : 14/05/1988 BEYKOZ/ISTANBUL  
**Foreign Languages** : English - Italian  
**E-mail** : turgaycaglar88@yahoo.com

### EDUCATION

<b>Degree</b>	<b>Department</b>	<b>University</b>	<b>Date of Graduation</b>
Master	Physics	Yıldız Technical University	01/2016
Undergraduate	Physics	Kocaeli University	07/2011